Research Article

Nano Research
2022, 15(5): 4164–4174

ISSN 1998-0124 CN 11-5974/O4
https://doi.org/10.1007/s12274-021-3998-3

Intelligent bio-assembly imaging-guided platform for real-time bacteria sterilizing and infectious therapy

Jiayu Zeng[1,§], Zengchao Guo[1,§], Yihan Wang[1], Zhaojian Qin[1], Yi Ma[3], Hui Jiang[1], Yossi Weizmann[2] (✉), and Xuemei Wang[1] (✉)

[1] *State Key Laboratory of Bioelectronics (Chien-Shiung Wu Lab), School of Biological Science and Medical Engineering, Southeast University, Nanjing 210096, China*
[2] *Department of Chemistry, Ben-Gurion University of the Negev, Beer-Sheva 8410501, Israel*
[3] *Department of Engineering, China Pharmaceutical University, Nanjing 211198, China*
[§] *Jiayu Zeng and Zengchao Guo contributed equally to this work.*

Received: 11 October 2021 / **Revised:** 11 November 2021 / **Accepted:** 14 November 2021

ABSTRACT

Bacterial infection is rising as a threatening health issue. Because of the present delay in early diagnosis of bacterial diseases as well as the abuse of antibiotics, it has become a vital issue in the development of in-time detection and therapy of bacterial infections. Herein, we designed a multifunctional nanotheranostics platform based on the unique micro-environment of bacterial infections to achieve specific bioimaging and simultaneous inactivation of the target bacteria. We showed that in bacterial infections, the metal precursors (i.e., $HAuCl_4$, $FeCl_2$, and herring sperm DNA) could be readily bio-self-assembled to multifunctional nanoclusters (NCs) that exhibit luminescence, in which $AuCl_4^-$ was biosynthesized via reductive biomolecules such as NADPH to the fluorescent AuNCs. The DNA may assist as an encapsulation and delivery vector, and Fe^{2+} served as a fluorescence intensifier and reduced reactive oxygen species (ROS) to produce the iron oxides. While the bacteria were being visualized, the microenvironment-responsive NCs were enabled to sterilize bacteria efficiently due to electrostatic effect, cell membrane destruction, inhibition of biofilm formation, and ROS accumulation. Besides, the bio-responsive self-assembled NCs complexes contributed to accelerating bacteria-infected wound healing and showed negligible side effects in long-term toxicity tests *in vivo*. Also, intracellular molecules involved in microenvironmental response were investigated. The work may become an effective strategy for the detection and real-time sterilization of intractable bacterial infections.

KEYWORDS

bacterial microenvironment response, self-assembled Fe@Au–DNA complexes, bacterial fluorescence bioimaging, bacteria inactivation, wound healing

1 Introduction

Bacterial infection has become a leading cause of numerous diseases, and especially, the formation of bacterial biofilms that accelerates their development poses a threat on human's lives [1, 2]. Traditional antibacterial agents such as antibiotics have been widely used to combat pathogens. However, caused by the off-label abuse due to insufficient surveillance, an emergent crisis of ongoing explosion and spread of antibiotics has erupted [3]. Worst still, because of the lack of bacteria diagnosis platforms [4, 5], it is challenging to monitor infections as well as real-time evaluation of therapeutic effectiveness, resulting in insufficient or delayed bactericidal treatment [6]. Therefore, facile and accurate detection or identification of bacteria becomes a vital issue in clinical medicine [7]. Till now, due to the less-developed techniques, the universal approaches for identifying bacteria are still either conventional plating and cultures, or genomic and immunological techniques [8, 9], which are time-consuming, costly, and instrument-dependent [10]. In this regard, it is imperative to accelerate the development of diagnostic strategies to facilitate antibiotic stewardship and optimize infection therapy [11]. In the last few years, the fluorescence imaging technique is emerging as a promising instrument applied in visualization and positioning of organisms due to its extensive superiority, such as high sensitivity and resolution, rapid responsiveness, and simplicity [12–14]. And recent advances confirm that fluorescence imaging has successfully been applied to the detection of bacteria *in vitro* and *in vivo* [15].

Among the nanomaterials applied in sensing and imaging, gold materials have attracted extensive attention with merits of fluorescence characteristics, quantum size effect, unique catalytic activity, surface-enhanced Raman scattering effect (SERS), photothermal effect, and good biocompatibility [16, 17]. Remarkably, fluorescence is one of the most prominent properties of gold nanoclusters (Au NCs) [18–20]. Au NCs are generally composed of several to hundreds of gold atoms with sizes commensurate to the Fermi wavelength of electrons, endowing it the molecular-like properties [20]. With advantages of strong luminescence, relatively long lifetime, simple synthesis, and favorable water solubility and biocompatibility, Au NCs enjoys a

Address correspondence to Yossi Weizmann, yweizmann@bgu.ac.il; Xuemei Wang, xuewang@seu.edu.cn

growing popularity in analytical and biomedicine applications [21–22], including theranostics of bacterial infections [23]. Templates or ligands are critical to the preparation of Au NCs with ultrasmall size [24]. Inspired by the "bioinspired synthesis" strategy, the reducing bio-macromolecules (such as proteins, thiolate ligands, and DNA) have served as the template for the synthesis and stabilization of the Au NCs, which aims to substitute natural and safer biomolecules for the use of aggressive chemicals and solvents [25]. It has been reported that the physicochemical characteristics of DNA make it accessible to metal connections, in which the practicability of specific base pairs and free radicals is conducive to the assembly and synthesis of particles [26, 27].

The bacterial microenvironment has become a suitable target for particular recognition and therapy of relative infectious illnesses due to its discrepancy compared with normal tissues [28], for example, hypoxia, higher glutathione (GSH)/oxidized GSH (GSSG) and $NADP^+$/NADPH [29]. Giao et al. also demonstrated the ubiquitous reducing power of bacteria; the electron transfer in the respiratory cascade of bacteria during normal bacterial proliferation would cause a significant drop in bulk redox potential (Eh) [30]. Besides, the reduction of metal ions of bacteria to form nanostructures belongs to self-help behavior that involves bio-concentration and bio-mineralization [31]. Based on the merits of microenvironment-responsive nanotheranostics, we have explored the bio-responsive self-assembly of Au NCs based on bacterial microenvironment to facilitate facile bacteria bioimaging and simultaneous infection therapy.

In this work, we firstly mix gold precursor ($HAuCl_4$) with nucleic acid (natural double-stranded DNA (dsDNA) from herring sperm (< 50 bp), in which $HAuCl_4$ connects to nucleotides via the strong and specific metal-binding sites to form Au(III)–DNA complexes [32]. Subsequently co-cultured with bacteria, the Au(III) complexes are bio-reduced and self-assembled to fluorescence NCs. Besides, Fe^{2+} is introduced to enhance the fluorescence of Au NCs, which enables the creation of a more reductive microenvironment [33]. The new strategy replaces traditional fluorescent labels synthesized *in vitro*, eliminating the side effects of nanoparticle delivery, and improving the targeting and sensitivity of bioimaging. And the antimicrobial activity of ultrasmall Au NCs has been extensively investigated. Our studies demonstrate the microenvironment-responsive self-assembly can be used for accurate bacteria bioimaging and simultaneously infection therapy *in vitro* and *in vivo*.

2 Materials and methods

2.1 Materials and equipments

Chloroauric acid ($HAuCl_4$, CAS: 16903-35-8), Iron(II) chloride tetrahydrate ($FeCl_2{\cdot}4H_2O$, CAS: 13478-10-9), natural double-stranded DNA (dsDNA) from herring sperm (< 50 bp), the reactive oxygen species (ROS) kits, and the CCK-8 kits were purchased from Biyuntian Biotechnology Co., Ltd. (China). The interleukin (IL)-6 and tumor necrosis factor (TNF)-α enzyme linked immunosorbent assay (ELISA) kits were purchased from Thermo Fisher Scientific Co., Ltd. (China). The ROS scavengers: catalase, isopropanol, L-histidine, and 2,2,6,6-tetramethylpiperidine-1-oxyl (TEMPO) were all purchased from Shanghai Aladdin Bio-Chem Technology Co., Ltd. (China). The biofilm dye (crystal violet) was purchased from Vikki Biotechnology Co., Ltd. (China).

The transmission electron microscopic (TEM) images were characterized by a JEM-2100 microscope operating at 200 kV (JEOL, Japan). Energy dispersive spectroscopy (EDS) was characterized by a field-emission scanning electron microscope (SEM) (Zeiss, Ultra Plus). The fluorescent image of bacteria was visualized by a confocal microscope (Nikon INTENSILIGHT C-HGFIE). The zeta potential was acquired on a Zetasizer Nano ZSE (UK). The SERS spetroscopy was analyzed by a laser microscopic Raman spectrometer (inVia). The Fourier transform infrared (FITR) spetroscopy was characterized by a Thermo scientific, NICOLET iS5. The X-ray photoelectron spectroscopy (XPS) was measured by using PHI Quantera II with A1 Ka radiation (hv = 1, 486.6 eV). The fluorescence bioimaging study *in vivo* was record with optical imaging system for small animals (Perkin Elmer, *in vivo* optical imaging (IVIS) Lumina XRMS Series III).

2.2 Bacterial strains and culture

The bacteria species, *Escherichia coli* (ATCC35218) and *Staphylococcus aureus* (ATCC29213) were cultivated with lysogeny broth (LB) media. To obtain single isolated colonies, the bacteria were streaked onto LB agar plates and cultured in a constant temperature incubator at 37 °C overnight. Single bacterial colonies were cultured in 6 mL of LB shake bacteria tube and incubated at 37 °C for 8–10 h on a shaker (150 rpm). Freshly collected bacteria were used in each test.

2.3 Synthesis of microenvironmental-responsive NCs

AuNCs (Au): Bacteria (*E. coli* or *S. aureus*, OD = 0.2) were suspended in 1 mL of phosphate buffered saline (PBS) in PU tube, and then $HAuCl_4$ solution at a ultimate concentration of 100 μM was added to the culture. After fully mixing, the tube was incubated at 37 °C for 8 h on a shaker (150 rpm).

Au–DNA NCs (Au–DNA): Bacteria (*E. coli* or *S. aureus*, OD = 0.2) were suspended in 1 mL of PBS in PU tube, $HAuCl_4$ solution at a ultimate concentration of 100 μM and natural dsDNA from herring sperm (< 50 bp) (hsDNA) at a ultimate concentration of 20 μg/mL were then added to the culture. The tube was incubated at 37 °C for 8 h on a shaker (150 rpm) after fully mixing.

Au–Fe complexes (Au@Fe): Bacteria (*E. coli* or *S. aureus*, OD = 0.2) were suspended in 1 mL of PBS in PU tube, and then $HAuCl_4$ solution at an ultimate concentration of 100 μM was added. After 10 min, $FeCl_2$ liquor at an ultimate concentration of 100 μM was added to the culture. The tube was incubated at 37 °C for 8 h on a shaker (150 rpm) after fully mixing.

Fe complexes (Fe): Bacteria (*E. coli* or *S. aureus*, OD = 0.2) were suspended in 1 mL of PBS in PU tube, and then $FeCl_2$ solution at an ultimate concentration of 100 μM was added to the culture. The tube was incubated at 37 °C for 8 h on a shaker (150 rpm) after fully mixing.

Fe DNA complexes (Fe DNA): Bacteria *(E. coli* or *S. aureus*, OD = 0.2) were suspended in 1 mL of PBS in PU tube, $FeCl_2$ solution at an ultimate concentration of 100 μM and hsDNA at an ultimate concentration of 20 μg/mL were then added to the culture. The tube was incubated at 37 °C for 8 h on a shaker (150 rpm) after fully mixing.

Au–DNA–Fe complexes (Fe@Au–DNA): Bacteria (*E. coli* or *S. aureus*, OD = 0.2) were suspended in 1 mL of PBS in PU tube, $HAuCl_4$ precursors at a ultimate concentration of 100 μM and hs DNA at a ultimate concentration of 20 μg/mL were then added to the culture, after 10 min, introduced $FeCl_2$ solution at a ultimate concentration of 100 μM to the culture. The tube was incubated at 37 °C for 8 h on shaker (150 rpm) after fully mixing.

2.4 Extraction of self-assembled NCs in bacteria

The extraction of as-prepared bioresponsive nanoclusters were carried out according to the procedure of previous work. After 8 h of incubation (AuNCs had been already synthesized), the LB media was removed, and bacteria were rinsed with deionized

water three times. Then bacteria were damaged using an ultrasonic cell crusher for 15 min. And freeze–thaw method was used to further crush the cells via immersing in liquid nitrogen (5 min at –180 °C) and water bath (15 min at 37 °C) for cell lysis, and then the lysed tissue solution was centrifuged at 8,000 rpm for 10 min. The supernatant was collected, and the self-assembled nanoclusters were used for further characterization.

2.5 Antimicrobial test *in vitro*

Agar plate assays were tested to evaluate the antibacterial activity of self-assembled NCs. In this work, 8 different formulation groups were chosen: PBS, free DNA (20 μg/mL DNA), Au (100 μM $HAuCl_4$ solution), Au–DNA (100 μM $HAuCl_4$ solution, 20 μg/mL DNA), Fe (100 μM $FeCl_2$ solution), Fe DNA (100 μM $FeCl_2$ solution, 20 μg/mL DNA), Au@Fe (100μM $HAuCl_4$ solution, 100 μM $FeCl_2$ solution), Fe@Au–DNA (100 μM $HAuCl_4$ solution, 100 μM $FeCl_2$ solution, 20 μg/mL DNA). Each group was co-cultured with unsalted *E. coli* and *S. aureus* solutions (~ 1.0×10^8 colony-forming unit (CFU)/mL) for 8 h in the oscillator at 35 °C. Then 100 μL of 10^6-diluted mixture was dropped onto a solid LB agar plate. After 24 h of cultivation, the number of colonies was recorded.

2.6 Observation of bacterial morphology

The morphological changes of bacteria were observed by SEM. A certain concentration of *E. coli* was treated by 8 different groups for 8 h, respectively, and then was centrifuged at 2,000 rpm for 5 min. The supernatant was used to collect bacteria and deionized with sterile water 3 times. The cleaned bacteria were fixed with 2.5% glutaraldehyde for 1.5 h and then dehydrated with 30%, 50%, 70%, 90%, and 100% ethanol sequentially, and finally, their morphology was observed by Zeiss Ultra Plus SEM.

2.7 Evaluation of inhibition of bacterial biofilms

E. coli (initially OD = 0.1) treated with different metal precursors was put into a 96-well plate and cultured at 37 °C for 2 days. After being cleaned by PBS for 3 times, 0.1% crystal violet was added into each well of the plate and stained for 10 min, followed by washing twice with deionized water. Finally, the dye attached to the biofilm was dissolved by adding 200 μL of absolute C_2H_5OH. And a microplate reader was used to measure the ultraviolet (UV) absorption intensity at 595 nm.

2.8 ROS Measurement

For the ROS assay, the ROS of different groups were measured with a Reactive Oxygen Detection Kit (S0033, Beyotime).

2.9 Quantitative evaluation of GSH in *E. coli* with different treatments

E. coil with different treatments were collected as described in the previous experiments, and the concentrations of intracellular GSH were measured by using a commercial GSH kit from Nanjing Jiancheng Bioengineering Institute. The detailed procedures were operated according to the instructions. The absorbance of 5,5′-dithiobis(2-nitrobenzoic acid) (DTNB) at 420 nm can be employed to evaluate the GSH level of the sample.

2.10 Quantitative evaluation of $NADP^+$/NADPH in *E. coli* with different treatments

E. coli with different treatments were collected as described in the previous experiments, and the concentrations of intracellular NADPH and $NADP^+$ were measured by using a commercial NADP(H) kit from Nanjing Jiancheng Bioengineering Institute. The detailed procedures were operated according to the instructions. The oxidized thiazolium blue could be reduced to formazan by NADPH through the hydrogen transfer of peroxymonosulfate (PMS), whose absorbance at 570 nm can be employed to evaluate the NADP(H) level of the sample.

2.11 The CCK8 cytotoxicity assay

A total of 10^4 cells were plated in 200 μL of complete cell culture media per well in a 96-well plate. And cells were divided into eight distinct groups: DNA, Au, Au–DNA, Fe, Fe DNA, Au@Fe, and Fe@Au–DNA group. In the DNA group, cells were treated with DNA (100 μL, 20 μg/mL). In the Au group, 100 μL of $HAuCl_4$ precursor with a concentration gradient of 20, 40, 80, 160, 320, 640, 1,280, and 2,560 μmol/L were added in each 3 wells (n = 3). Analogously, the same steps were adopted for $FeCl_2$ in the Fe group. In the Au–DNA group, cells were co-cultured with 20 μg/mL DNA and Au ions with various concentrations of 20, 40, 80, 160, 320, 640, 1,280, and 2,560 μmol/L for 100 μL. Likely, in the Fe DNA group, the same steps were adopted for $FeCl_2$ and DNA solutions. In the Au@Fe experimental group, initially 50 μL of $FeCl_2$ with concentration gradient of 20, 40, 80, 160, 320, 640, 1, 280, and 2,560 μmol/L was added, 10 min later, 50 μL of $HAuCl_4$ with the same concentrations as for $FeCl_2$ was added. In the Fe@Au–DNA treatment group, cells were firstly treated with 20 μg/mL DNA and $FeCl_2$ with a concentration gradient of 20, 40, 80, 160, 320, 640, 1,280, and 2,560 μmol/L for 50 μL, 10 min later, 50 μL of DNA and $HAuCl_4$ solutions with the same concentrations as for $FeCl_2$ were introduced. The control group was only placed in the Dulbecco's modified Eagle medium (DMEM), while other conditions remained unchanged. After 1 day, 100 μL of CCK8 solution was added into each well of the plate ($V_{CCK\text{-}8}$:V_{medium} = 1:9) and co-cultured for an accessional 2 h. And then a microplate reader was used to measure the absorbance of each well at a wavelength of 450 nm to indirectly detect cell activity and proliferation.

2.12 Bacteria-infected animal models

All the animal experiments in this study were referred to the Guidelines for the Care and Use of Laboratory Animals, and were conducted under the supervision of the Animal Ethics Committee of Southeast University. The female Kunming (KM) mice (20 g, one-month-old), as the subject of the experiment, were obtained from Nanjing Qinglongshan Animal Farm (China). To make the *E. coli*-infected mice model, the rats were gas-ether anesthetized by isoflurane and marked by a partial-thickness openning of 1 cm in diameter in the backbones. Then the prepared wounds were treated with 50 μL of *E. coli* (1.0×10^9 CFU/mL). After being treated for 1 day, the treated mice developed subcutaneous abscesses, suggesting the forming of bacterial infections.

2.13 Fluorescence imaging of bacteria-infected mice

Fluorescence imaging of mice *in vivo* (excited at 480 nm and emitted at 670 nm) was performed using the PerkinElmer IVIS (Lumina XRMS Series III). It also set eight treatment groups (PBS, DNA, Au, Au–DNA, Fe, Fe–DNA, Au@Fe, and Fe@Au–DNA), and the concentration of metal precursors was tripled as that *in vitro* ($HAuCl_4$: 300 μM; $FeCl_2$: 300 μM; hsDNA: 60 μg/mL). The wounds of mice for each group were covered with 50 μL of corresponding ion suspensions (while using 50 μL of PBS for the control group). In the experiment, mice were subjected to general anesthesia with 5% isoflurane in an air-obsessed manner and bio-imaged at specific time points of pre-daub (0 h) and post-daub for 2, 6, 12, 24 h, and 15 days.

2.14 Treatment of bacterial infection in mice

Similarly, the KM mice infected by *E. coli* were divided into 8 groups of different treatments, and the wounds of mice for each

group were covered with 50 μL of corresponding ion suspensions with the same concentration as in the test in Section 2.11 for three times (at day 1, 3, and 5, respectively). During the cure, wounds were photographed, and body weight of each mouse was recorded. After 15 days of treatment, all mice were sacrificed. The size of infected wound was measured with a ruler with an interval of two days, and was counted by the following equation: Area = (width/2 × length/2) × π. Besides. The serum was collected for enzymes tests, including IL-6 and TNF-α for inflammatory response assessment. To further evaluate the long-term toxicity of the materials, the skins, and organs of each group of mice were treated with hematoxylin and eosin (H&E) staining for histological analysis.

3 Results and discussion

3.1 Characterization of environment-responsive AuNCs complexes

For intracellular gold nanoparticle formation, it is better to deploying ionic gold in discrete nanoscale packets to reduce the caustic properties of gold precursors, because it saved reaction time, and most importantly, minimize the influence on cellular health [34]. In this work, we have exploited the possibility to utilize natural dsDNA from herring sperm (< 50 bp) to serve as the ionic gold package and delivery vehicle [35]. As illustrated in Fig. S1(a) in the Electronic Supplementary Material (ESM), ionic Au^{3+} and Fe^{2+} can be easily attached to DNA due to electrostatic interaction. And it is more certain that Au^{3+} binds to DNA with Au's proven specific binding site [36]. It can be observed that after complexation of DNA with Au^{3+} and Fe^{2+} ions, the relevant surface charges significantly changed, and its potential value became positive 6.57 mV, endowing it more accessible to negatively charged *E. coli* or *S. aureus* in PBS with pH = 7.2. More importantly, the positively charged metal precursor enabled to compromise bacterial membrane because of charge neutralization, leaving some holes on the cell membrane surface, which facilitated the entry of DNA complexes.

To confirm the formation of gold nanoclusters (AuNCs), the microenvironment-responsive NCs have been extracted from *E. coli* cells for further characterization. It demonstrated the existence of AuNCs with a diameter of 2.48 ± 0.54 nm and Au–DNA NCs with a diameter of 2.24 ± 0.52 nm from the TEM image and the particle size distribution curve (Figs. 1(b) and 1(d), Figs. S3(a) and S3(b) in the ESM). The AuNCs interplanar distance was found to be 0.235 nm, corresponding to (111) planes of AuNCs (Fig. 1(c)). As illustrated in Fig. 1(h) and Fig. S2 in the ESM, it showed EDS results of bacterial extractions of each group to detect intracellular iron and gold ions. The amount of Au and Fe slightly increased in the presence of DNA between the parallel groups, indicating that DNA could be utilized as an effective carrier for metal cations delivery. In this system, Fe^{2+} was probably converted to iron oxides (Figs. 1(e)–1(g)), for Fe^{3+} improves the reducibility of the bacterial microenvironment. An XPS of the extract of Fe@Au–DNA was performed to further illustrate the valence states of intracellular gold and iron (Figs. 1(i) and 1(j)). The XPS spectra of Au4f can be fitted into two groups of double peaks, in which the peaks of 87.16 and 83.56 eV are derived from Au(0), corresponding to $Au4f_{5/2}$ and $Au4f_{7/2}$, respectively. While the double peaks at 87.90 and 84.29 eV belong to the photoelectron emission of $Au4f_{5/2}$ and $Au4f_{7/2}$ of Au(I). An Au(0) and Au(I) contributed 64.67% and 35.33%, respectively. Similarly, the two peaks of XPS spectra of Fe2p corresponded to $Fe2p_{1/2}$ and $Fe2p_{3/2}$, respectively, demonstrating Fe(+2) and Fe(+3) coexisted in the sample with the contribution of 57.35% and 42.65%, respectively.

In addition, FTIR and SERS were applied to examine the interaction between the metal ions and DNA in bio-assembled gold nanoclusters complexes. As shown in Fig. S4(a) in the ESM, the infrared spectra of the extract of *E. coli* with different treatments showed significant distinctions. The characteristic peaks of free DNA at about 1,686, 1,529, and 1,488 cm^{-1} correspond to C=O, $C=N_{imine}$, and cytosine (C), respectively [37–39]. Their position or peak intensities were changed at Au–DNA and Fe@Au–DNA groups, indicating that the attachment of AuNCs affected the structure of DNA. In Fig. S4(b) in the ESM, some characteristic peaks showed different levels of enhancement of Raman signal assigned to the vibration absorption of several DNA bases and deoxyribose skeleton [35], which can be explained by the interaction between the relevant group of DNA and metal ions.

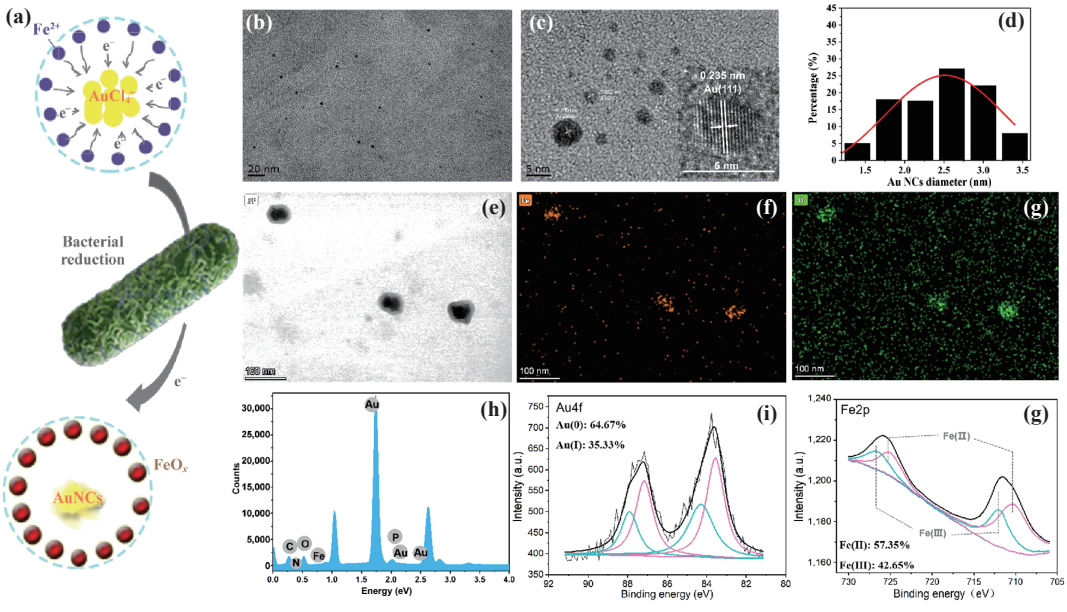

Figure 1 Characteristics of in situ bio-self-assembled NCs. (a) Schematic illumination of the synthesis of AuNCs via bacterial reduction. Typical TEM image of (b) isolated gold nanoclusters and (c) high resolution (HR)-TEM image of gold nanoclusters. The statistical results of the particle-size distribution of NCs are shown in (d). (e) HAADF-STEM characterization of the bioresponsive FeO_x nanoparticles, with EDS mapping (f) and (g) on the TEM grid of (e). (h) EDS spectrum of the extract of Au@Fe group. (i) Au4f and and (j) Fe2p XPS spectra of Au nanoclusters and FeO_x complexes.

3.2 Fluorescence bioimaging study

The fluorescence bioimaging effect was initially evaluated via confocal fluorescence microscopy for *E. coli* and *S. aureus* treated with different metal precursors. A pre-experiment found little linear correlation between $HAuCl_4$ concentration and fluorescence intensity (Fig. S5 in the ESM). Considering the cell biocompatibility and antibacterial properties, we chose 100 μM gold precursor as the optimal concentration. In this experiment, $HAuCl_4$ (100 μM) with/without hsDNA (20 μg/mL) was added into the PBS for Fe@Au and Fe@Au–DNA groups, $FeCl_2$ (100 μM) was also added after 10 min. Then the metal precursors were incubated with *E. coli* and *S. aureus* for 8 h, while for the control groups, only PBS or DNA was used. As shown in Fig. 2(a) and Fig, S6 in the ESM, bright fluorescence had emerged in bacteria treated with gold precursors, which demonstrated successfully bio-assembly of fluorescent Au NCs and well distribution of almost all target bacterial cells. Nevertheless, slight fluorescence was detected in PBS and DNA groups. Fe and Fe DNA groups showed a weak fluorescence, probably attributing to bacteria's autofluorescence when treated with exogenous metal ions [39]. However, it could be negligible compared with NCs with notable luminescence. When Fe^{2+} was introduced in the system, it obtained a stronger fluorescence intensity of cells (Figs. 2(b) and 2(c)), for Fe^{2+} also contributes to the reduction of Au^{3+}. Our team has clarified the redox mechanism of Au(III)–Fe(II) system by simulating the interaction and transformation of Fe^{2+}, Au^{3+}, and reductive substance (use GSH as an example) through *in vitro* tests, which illustrated the rationality of adding Fe^{2+} [40]. It is clear that DNA also benefits the fluorescence enhancement as the delivery carrier of ionic metals. Meanwhile, quantitative variations in relative fluorescence intensity of each group's representatively single bacterium were further compared to exhibit the distinction of fluorescence intensity more intuitively within the bacterium.

3.3 Antibacterial activities and potential mechanism in the process of self-assembled NCs

The favorable antibacterial effects praise AuNCs as promising inactivated materials to compete with bacterial infections [40]. The

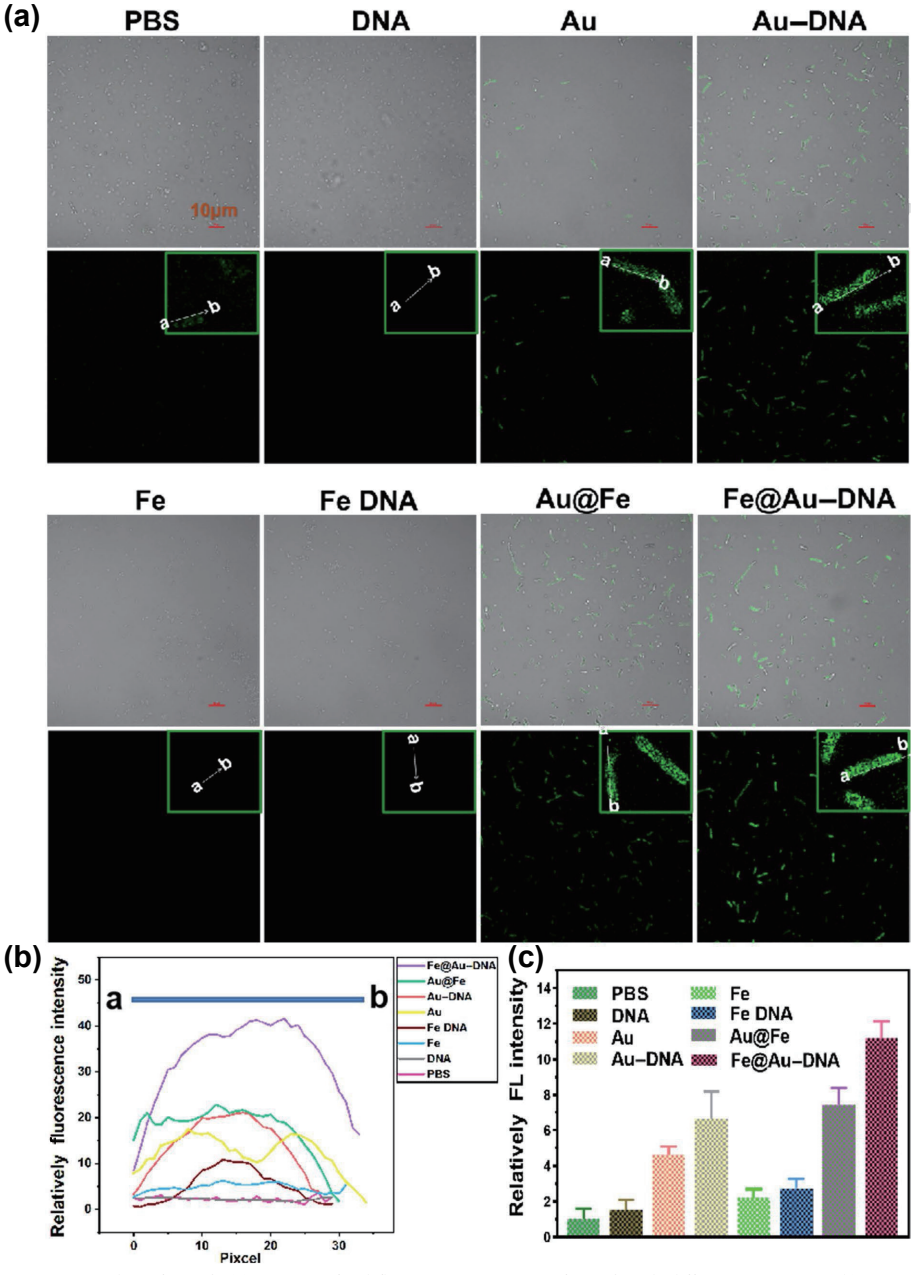

Figure 2 Fluorescence bioimaging studies of *E. coli*. (a) Laser confocal fluorescence imaging of *E. coli* with different treatments. (b) Quantitative analysis of relative fluorescence intensity of cell lines, and (c) total cells as shown in (a).

antibacterial activity of bio-responsive self-assembly was also investigated in this study. The optimal concentration of metal precursors with/without hsDNA mentioned above was co-cultured with *E. coli* (initial OD = 0.1) for 8 h. As depicted in Figs. 3(b) and 3(c), groups with metal complexes all exhibited excellent antibacterial activity that reached 80%. It is clear that the introduction of DNA slightly decreased the inhibition of bacteria, suggesting this exogenous gene showed good cytocompatibility, which could also be proved in Fig. S10 in the ESM. Under the synergy effect of bimetal, the antibacterial capability was greatly improved to 95%. Also, as shown in Fig. 3(d), cytoderm and membranes had been severely destroyed in metal groups compared with the control (PBS and DNA groups). For one thing, positively charged metal precursors could damage cell membrane via electrostatic interaction; more importantly, the bio-self-assembled AuNCs contributed to bacterial disinfection. Previous research proved that ultrasmall AuNCs are antimicrobic, while their larger counterparts Au NPs had no inactivation activity, for internalized AuNCs were enabled to induce ROS that caused oxidative stress damage [41]. Consistent with this conclusion, it also exhibited the induction capability of ROS in this study. Intracellular ROS of *E. coil* with different treatments was indirectly detected by fluorescent DCFH-DA probe, which excites at 488 nm and emits at 525 nm (Fig. S7 in the ESM). Compared with the control that labeled as 1, *E. coil* treated with metal complexes showed a higher ROS level (Fig. 3(e)). It is evident that Au and Au–DNA groups produced more ROS than counterpart Fe's, which indirectly proved the microenvironment-response of AuNCs required the consumption of intracellular reducing substances, while the oxidation levels were accordingly increased. The ROS levels of Au@Fe and Fe@Au–DNA groups were significantly higher, demonstrating the efficient self-assembled of AuNCs in the presence of Fe^{2+}. Moreover, as shown in Fig. 3(f), the bio-responsive NCs could synergistically eliminate biofilm formed by *E. coli*.

Furthermore, four scavenger-quenching tests were conducted to investigate the disinfection contribution of each ROS (Fig. 3(g) and Fig. S8 in the ESM). It can be seen that scavengers exerted little influence in the growth of bacteria in the control group (Fig. S8 in the ESM), which suggested it was species of ROS rather than scavengers-made effects on bacterial sterilization. Comparing with Fe@Au–DNA without scavenger group, which showed almost 100% of antibacterial rate after 24 h incubation, it presented four ROS ($O_2^{\cdot-}$, $^1O_2$, H_2O_2, and ·OH) with contributions to H_2O_2>>·OH > $^1O_2$ > $O_2^{\cdot-}$ in the system. It is reported that AuNCs can act as like-peroxidases that oxidizes the intracellular substrate and meanwhile reduces O_2 to H_2O_2 (Fig. 3(a)) [42]. The associated redox reactions are listed as follows, in which Fe(II) enables to trigger to produce highly toxic ·OH [43].

$$RH_2 + O_2 \xrightarrow{AuNCs} RH_2 + O_2\,(RH_2\text{refers} \rightarrow \text{substrate}) \quad (1)$$

$$H_2O_2 + Fe\,(II) \rightarrow \cdot OH + Fe\,(III) \quad (2)$$

$$O_2 \rightarrow {}^1O_2 \quad (3)$$

$$O_2 + Fe\,(II) \rightarrow O_2^{\cdot-} + Fe\,(III) \quad (4)$$

$$O_2^{\cdot-} + H_2O \rightarrow 1O_2 + H_2O_2 + 2OH^- \quad (5)$$

According to previous researches, the bio-synthesized AuNCs seeds acted as catalysts to reduce $AuCl_4^-$ by H_2O_2 to further generate more AuNCs [44] and the new-generated O_2 can be used in Eq. (1).

$$AuCl_4^- + \frac{3}{2}H_2O_2 \rightarrow Au^0 + 4Cl^- + 3H^+ + \frac{3}{2}O_2 \quad (6)$$

3.4 Investigation on participating biomolecules in bioresponsive self-assembly

To better understand the inner mechanism of bio-responsive process, we identified cellular biomolecules that might be involved in biological reduction. GSH, a typical reductive biomolecule in the bacterial microenvironment, has been widely used as ligand to synthesize AuNCs *in vitro* [45]. GSH may be depleted to bio-synthesized NCs in bacterial infections. However, as shown in Fig. 4(a), it surprisingly proved that GSH did not participate in the bioresponsive self-assembly, because the concentration of GSH in the experimental groups did not decrease but increase when compared with the control group (PBS, DNA). The increase of GSH can be attributable to the cellular defense against over-high ROS. Later, another reductive biomolecule NADPH was also investigated (Fig. 4(b)). It is reported that ratio of

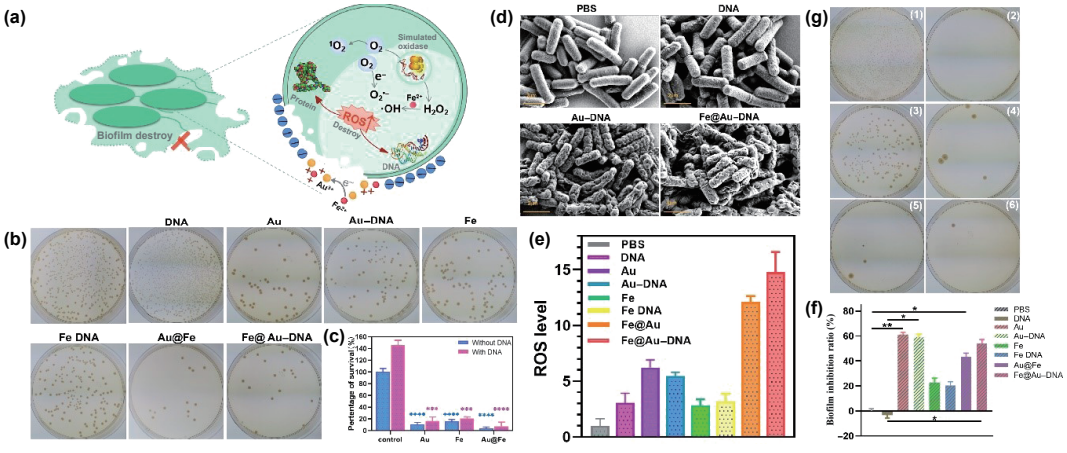

Figure 3 Antibacterial testing for the process of bio-responsive self-assembled NCs. (a) The antibacterial mechanism in the process of self-assembled NCs. (b) Photographs of the agar plates and (c) the corresponding statistical histogram of *E. coli* colonies of each group. No duplicated two-factor analysis of variance was applied to evaluate various mean distinction. ***p < 0.001, ****p < 0.0001. (d) SEM micrographs of *E. coli* cells without treatment (control) and with different treatments. Scale bar, 2 μm. (e) The normalization of measure of cellular ROS levels with fluorescent DCFH-DA probe, while the ROS level of the control (PBS) is labeled as 1. (f) The biofilm inhibition ratio of *E. coli* with different treatments. *p < 0.05, **p < 0.01. (g) ROS scavenger quenching test for *E. coli* treated with $FeCl_2$, $HAuCl_4$ and DNA complexes (Fe@Au–DNA group) for 24 h, among which *E. coli* were incubated with (1) PBS, (2) mixtures of ionic precursors (Fe@Au–DNA), (3) Fe@Au–DNA and catalase (H_2O_2 scavenger), (4) Fe@Au–DNA and isopropanol (·OH scavenger), (5) Fe@Au–DNA and L-histidine ($^1O_2$ scavenger), and (6) Fe@Au-DNA and TEMPO ($O_2^{\cdot-}$ scavenger), respectively.

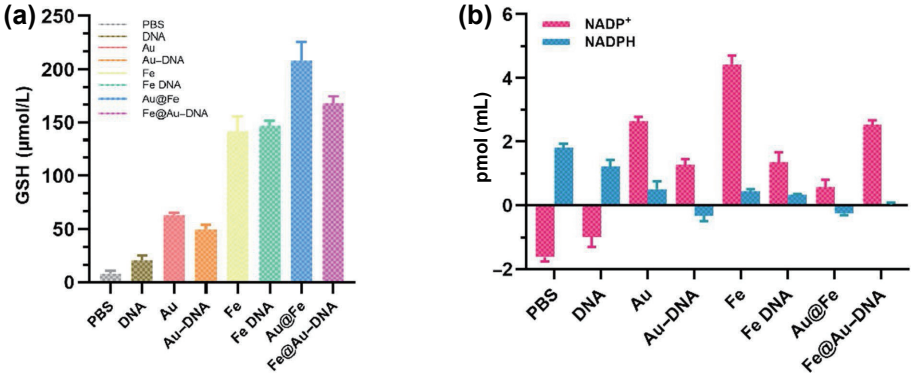

Figure 4 The concentration of GSH (a) and NADP⁺/NADPH (b) of *E. coli* treated with different treatments.

NADPH/NADP⁺ is the main indicator of the redox state of cells and plays an important regulatory role in biosynthesis and antioxidant metabolism [46]. It can be seen that NADPH positively involved in biological reduction of metal precursors, for the partly NADPH was consumed and converted into NADP⁺. Some of the values are negative due to their concentration being less than the reference. According to the previous researches, proteins would be progressively accumulated as the ionic gold entered the cells, which had been proven to be involved in intracellular reduction of $HAuCl_4$ [33].

3.5 Bio-responsive self-assembly AuNCs complexes in bacteria bioimaging *in vivo*

It was necessary to analyze the cytocompatibility of the metal precursors before *in vivo* experiments. The cellular toxicities of Au and Fe ions with/without DNA on human normal liver L02 cells were evaluated using CCK-8 assay via quantification of viable cells to evaluate the preliminary bio-compatibility (Fig. 5(b)). It was clear that metal ion solutions displayed concentration-dependent cytotoxicity. The cells in each group exhibited a survival rate higher than 80% in the concentration range of 320 μM. The Fe ion solution showed much better biocompatibility than that of Au above 320 μM and displayed a survival rate higher than 70%. Compared with the single metal ion solution, the cytotoxicity of Au@Fe did not show the additive effect of both, probably for the redox reaction between both neutralized parts of the ion toxicity.

To further understand and evaluate the fluorescence imaging effect of the bio-responsive AuNCs complexes *in vivo*, we established a female KM mice model and randomly divided the mice into 8 groups (3 mice per group). Before optical imaging *in vivo*, the tested mice were completely depilated to eliminate the interference of hair on the target imaging signal [47, 48]. A wound of 1 cm in diameter was created by scissors in each mouse and subsequently covered with 50 μL of *E. coli* (initially OD = 1) to develop bacterial infections. After one day, the mice in each group were treated with 50 μL of different precursors, and the concentration of precursors was tripled as that *in vitro*, followed by one mouse in each group randomly selected for *in vivo* fluorescent imaging to examine the bacteria targeting effect of bio-synthesized complexes within 24 h (Fig. 5(a)). As shown in Fig. 5(c), Au, Au–DNA, Au@Fe, and Au@Fe–DNA groups all exhibited certain fluorescence in wounds after 6 h, which demonstrated the successful bio-assembly of fluorescent AuNCs complexes based on target infections. For comparison, there was no fluorescence at the wound site in the other groups. It was noticed that the non-wound parts of individual mice also showed some fluorescence, which can be attributed to the autofluorescence caused by the unremoved hair. As illustrated in Fig. 5(d), within the designed period of one day, the fluorescence intensity of the Au group initially enhanced and reached a maximum at approximately 12 h that cohered with the time required for bacterial bio-responsive self-assembly of AuNCs *in vitro*. And it decreased in the following period, probably attributing to the partial fluorescence quenching of NCs and the decrease of bacteria as a template (antibacterial effect of AuNCs). And it showed a stronger fluorescence intensity in the Au@Fe and Fe@Au–DNA groups, which further proved the effect of introducing Fe^{2+}. It can be seen that the fluorescence of each group was completely eliminated with wound healing after 15 days (Fig. S9 in the ESM).

3.6 *In vivo* treatment of bacterial infection

Eventually, the microenvironment-responsive self-assembly NCs was further evaluated for bacterial infection therapy and wound healing. As illustrated in Fig. 6(a), after the development of bacterial infections in the wound (the same as the method in previous fluorescence imaging experiment *in vivo*), the mice in each group were treated with 50 μL of different suspensions three times (at day 1, 3, and 5, respectively). Then the treatment was ended after 15 days. Wound size was measured every 2 days to evaluate the therapeutic efficacy (Fig. 6(b)). We observed that all the NCs groups' wounds were healed after 15 days of treatment except for the control (PBS), which demonstrated microenvironment-responsive probes' bactericidal abilities. Besides, it showed remarkable wound healing effects for the groups of Au–DNA and Fe@Au–DNA where the relative size of the wound area decreased rapidly (Fig. 6(c)), indicating that DNA contributes to the acceleration of healing. The therapeutic effect of the free DNA group was also better than that of the control PBS. As depicted in Fig. S10 in the ESM, the cell viability of hsDNA was 119.37% ± 10.94%, proving the exogenous DNA has favorable biocompatibility.

Furthermore, the long-term toxicity *in vivo* of bio-responsive nanotheranostics was also observed. It can be seen from Fig. 6(d) that the weight of mice in the experimental groups increased steadily and showed no evident differences, when compared with the mice of PBS group. To validate the inflammatory response in the process of microenvironmental self-assembly, the mice serum levels of IL-6 and TNF-α were tested after their sacrifice, which showed a certain increase in the acceptable range (Fig. 6(e)). Compared with the PBS, the H&E staining of wound region in other groups all showed different extents of hair follicle regeneration (Fig. 6(f)). And H&E staining pictures of main organs of the mice after 15 days of therapy exhibited no distinct injure or inflammatory affection (Fig. S11 in the ESM). These indicated the *in vivo* safety of the microenvironment- response to the self-assembly process.

4 Conclusions

In summary, in this paper, we have developed a facile multifunctional nanotheranostics strategy for bioimaging and real-

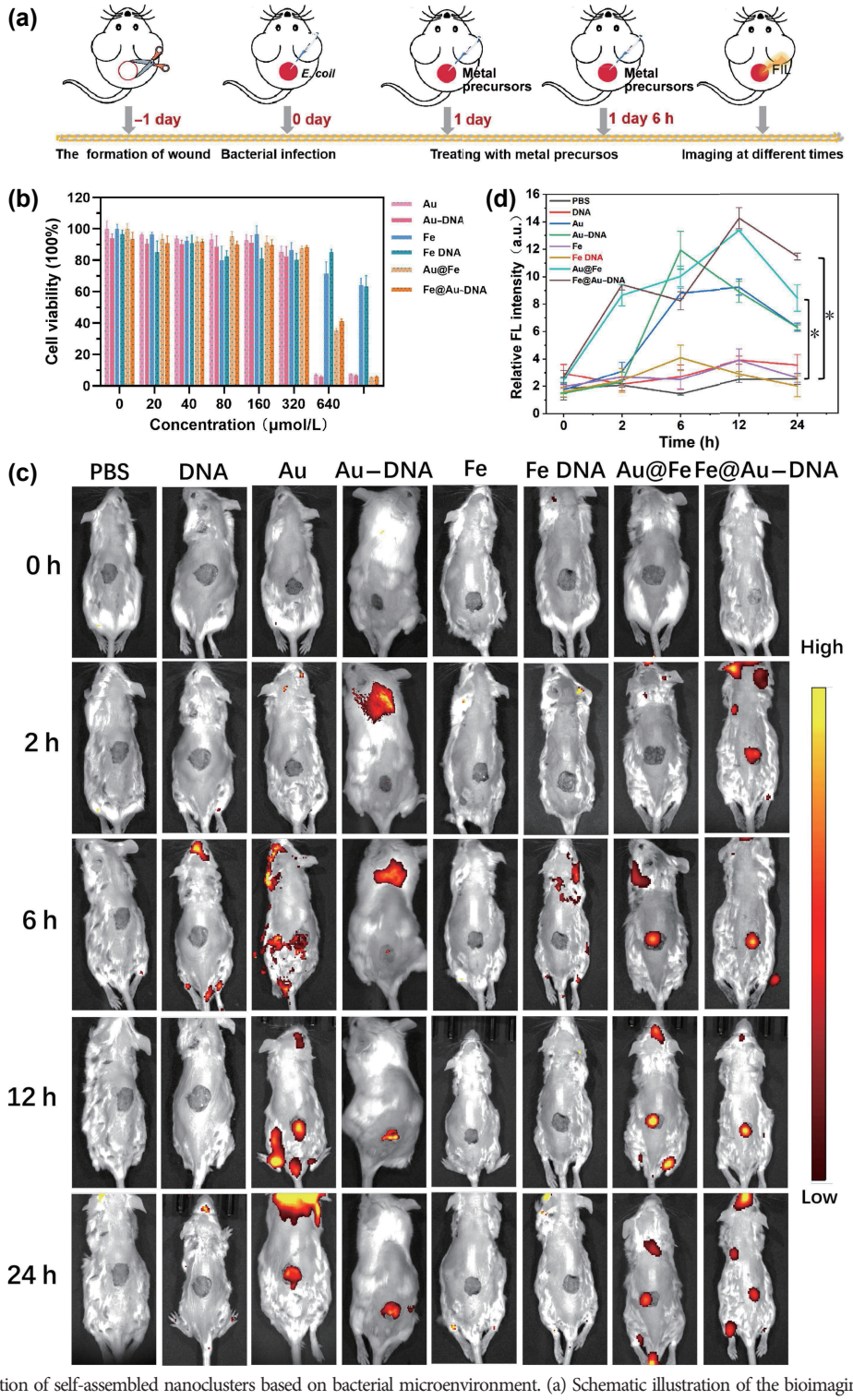

Figure 5 *In vivo* evaluation of self-assembled nanoclusters based on bacterial microenvironment. (a) Schematic illustration of the bioimaging of *E. coli*-infections in wounds by *in situ* daub of metal precursors. (b) *In vitro* cytotoxicity test for normal L02 cells in the presence of gold/iron solutions with or without DNA at various concentrations. (c) *In vivo* fluorescence photos of *E. coli*-infected KM mice after applying with 50 μL of different materials at different time points. (d) Curve of relative fluorescence intensity with time in mice as shown in (a). *$p < 0.05$.

time therapy of bacterial infections by bacterial microenvironment-responsive self-assembled gold nanoclusters. Metal precursors could be readily bio-reduced into biocompatible fluorescence NCs via unique microenvironment and physiological behavior of bacterial infections, in which NADPH/$NADP^+$ redox pair has been proven participation in the process. Also, the bio-responsive Au NCs is able to inactivate bacteria by electrostatic effect, destruction of the bacterial membrane, removal of bacterial biofilms, and generation of ROS. And the cells will accumulate more GSH in response to this oxidative stress. The specific process of microenvironment-responsive self-assembly has proved to be contributed to the acceleration of bacterial-infected wound healing, which shows the synergistic effects of both bacteria disinfection of nanoclusters and cell-proliferation promotion role of hsDNA. Furthermore, the bio-responsive self-assembly NCs shows no significant long-term toxicity in the animal-model study *in vivo*, suggesting further promising applications in medical fields. This research produces a promising multifunctional theranostic nanoplatform for specific visual diagnosis and concurrent therapy of bacterial infections.

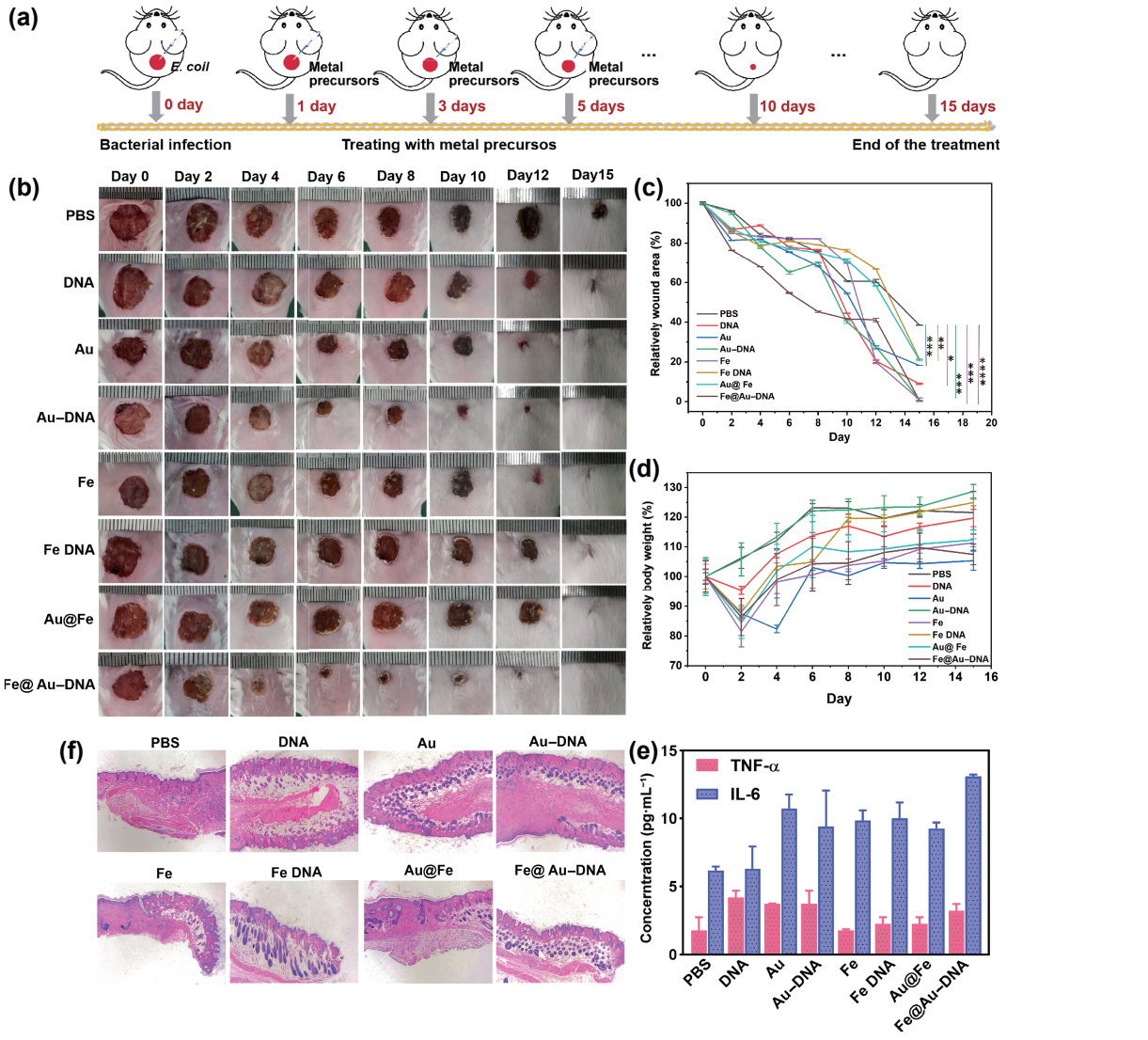

Figure 6 *In vivo* antibacterial evaluation by bio-responsive self-assembly NCs. (a) Schematic illustration of treatment strategies for bacterial wound infection. (b) Images of the *E. coli*-infected wounds from the mice of different groups in the interval of two days and (c) the corresponding changes in wound area after different treatments. $^{*}p < 0.05$, $^{**}p < 0.01$, $^{***}p < 0.001$, and $^{****}p < 0.0001$ (no repeated two-factor analysis of variance). (d) The body weight variation of mice. (e) The variation of cytokines (IL-6 and TNF-α) in mice serum after 15 days of antibacterial treatment. (f) The H&E staining of skin sections of wounds after 15 days of disparate therapy.

Acknowledgments

This work was supported by the National Key Research and Development Program of China (No. 2017YFA0205300), the National Natural Science Foundation of China (Nos. 82027806, 82061148012, and 91753106), Primary Research & Development Plan of Jiangsu Province (No. BE2019716), and the ISF-NSFC Joint Research Program (No. 3258/20) to Y. W.

Electronic Supplementary Material: Supplementary material (Figs. S1–S11) is available in the online version of this article at https://doi.org/10.1007/s12274-021-3998-3.

References

[1] Bing, W.; Chen, Z. W.; Sun, H. J.; Shi, P.; Gao, N.; Ren, J. S.; Qu, X. G. Visible-light-driven enhanced antibacterial and biofilm elimination activity of graphitic carbon nitride by embedded Ag nanoparticles. *Nano Res.* **2015**, *8*, 1648–1658.

[2] Zhao, Y.; Chen, L.; Wang, Y. A.; Song, X. Y.; Li, K. Y.; Yan, X. F.; Yu, L. M.; He, Z. Y. Nanomaterial-based strategies in antimicrobial applications: Progress and perspectives. *Nano Res.* **2021**, *14*, 4417–4441.

[3] Chatzopoulou, M.; Kyriakaki, A.; Reynolds, L. Review of antimicrobial resistance control strategies: Low impact of prospective audit with feedback on bacterial antibiotic resistance within hospital settings. *Infect. Dis.* **2021**, *53*, 159–168.

[4] Mills, B.; Bradley, M.; Dhaliwal, K. Optical imaging of bacterial infections. *Clin. Transl. Imag.* **2016**, *4*, 163–174.

[5] Mao, D.; Hu, F.; Kenry; Ji, S. L.; Wu, W. B.; Ding, D.; Kong, D. L.; Liu, B. Metal–organic-framework-assisted *in vivo* bacterial metabolic labeling and precise antibacterial therapy. *Adv. Mater.* **2018**, *30*, 1706831.

[6] van Oosten, M.; Hahn, M.; Crane, L. M. A.; Pleijhuis, R. G.; Francis, K. P.; van Dijl, J. M.; van Dam, G. M. Targeted imaging of bacterial infections: Advances, hurdles and hopes. *FEMS Microbiol. Rev.* **2015**, *39*, 892–916.

[7] Robby, A. I.; Kim, S. G.; Lee, U. H.; In, I.; Lee, G.; Park, S. Y. Wireless electrochemical and luminescent detection of bacteria based on surface-coated $CsWO_3$-immobilized fluorescent carbon dots with photothermal ablation of bacteria. *Chem. Eng. J.* **2021**, *403*, 126351.

[8] Zhou, C. C.; Xu, W. H.; Zhang, P. B.; Jiang, M. J.; Chen, Y. C.; Kwok, R. T. K.; Lee, M. M. S.; Shan, G. G.; Qi, R. L.; Zhou, X. et al. Engineering sensor arrays using aggregation-induced emission luminogens for pathogen identification. *Adv. Funct. Mater.* **2019**, *29*,

1805986.
[9] Lazcka, O.; Del Campo, F. J.; Muñoz, F. X. Pathogen detection: A perspective of traditional methods and biosensors. *Biosens. Bioelectron.* **2007**, *22*, 1205–1217.
[10] He, X. W.; Xiong, L. H.; Zhao, Z.; Wang, Z. Y.; Luo, L.; Lam, J. W. Y.; Kwok, R. T. K.; Tang, B. Z. AIE-based theranostic systems for detection and killing of pathogens. *Theranostics* **2019**, *9*, 3223–3248.
[11] Ren, C. H.; Wang, Z. Y.; Wang, Q.; Yang, C. H.; Liu, J. F. Self-assembled peptide-based nanoprobes for disease theranostics and disease-related molecular imaging. *Small Methods* **2020**, *4*, 1900403.
[12] Sun, X.; Zhang, M. Z.; Du, R. H.; Zheng, X. J.; Tang, C. G.; Wu, Y. Q.; He, J. C.; Huang, W.; Wang, Y. Y.; Zhang, Z. Y. et al. A polyethyleneimine-driven self-assembled nanoplatform for fluorescence and MR dual-mode imaging guided cancer chemotherapy. *Chem. Eng. J.* **2018**, *350*, 69–78.
[13] Zhao, S. J.; Wu, S. L.; Jia, Q. Y.; Huang, L.; Lan, M. H.; Wang, P. F.; Zhang, W. J. Lysosome-targetable carbon dots for highly efficient photothermal/photodynamic synergistic cancer therapy and photoacoustic/two-photon excited fluorescence imaging. *Chem. Eng. J.* **2020**, *388*, 124212.
[14] Liu, L.; Wang, X. Y.; Zhu, S. X.; Yao, C.; Ban, D. D.; Liu, R. H.; Li, L. D.; Wang, S. Controllable targeted accumulation of fluorescent conjugated polymers on bacteria mediated by a saccharide bridge. *Chem. Mater.* **2020**, *32*, 438–447.
[15] Váradi, L.; Luo, J. L.; Hibbs, D. E.; Perry, J. D.; Anderson, R. J.; Orenga, S.; Groundwater, P. W. Methods for the detection and identification of pathogenic bacteria: Past, present, and future. *Chem. Soc. Rev.* **2017**, *46*, 4818–4832.
[16] Guo, H. B.; Yi, S.; Feng, K.; Xia, Y. Q.; Qu, X. W.; Wan, F.; Chen, L.; Zhang, C. L. *In situ* formation of metal organic framework onto gold nanorods/mesoporous silica with functional integration for targeted theranostics. *Chem. Eng. J.* **2021**, *403*, 126432.
[17] Huang, Y.; Huang, P.; Lin, J. Plasmonic gold nanovesicles for biomedical applications. *Small Methods* **2019**, *3*, 1800394.
[18] Cui, H.; Shao, Z. S.; Song, Z.; Wang, Y. B.; Wang, H. S. Development of gold nanoclusters: From preparation to applications in the field of biomedicine. *J. Mater. Chem. C* **2020**, *8*, 14312–14333.
[19] El-Sayed, N.; Schneider, M. Advances in biomedical and pharmaceutical applications of protein-stabilized gold nanoclusters. *J. Mater. Chem. B* **2020**, *8*, 8952–8971.
[20] Zheng, J.; Nicovich, P. R.; Dickson, R. M. Highly fluorescent noble-metal quantum dots. *Annu. Rev. Phys. Chem.* **2007**, *58*, 409–431.
[21] Yarramala, D. S.; Baksi, A.; Pradeep, T.; Rao, C. P. Green synthesis of protein-protected fluorescent gold nanoclusters (AuNCs): Reducing the size of AuNCs by partially occupying the Ca^{2+} Site by La^{3+} in Apo-α-lactalbumin. *ACS Sustainable Chem. Eng.* **2017**, *5*, 6064–6069.
[22] Guo, Y. H.; Amunyela, H. T. N. N.; Cheng, Y. L.; Xie, Y. F.; Yu, H.; Yao, W. R.; Li, H. W.; Qian, H. Natural protein-templated fluorescent gold nanoclusters: Syntheses and applications. *Food Chem.* **2021**, *335*, 127657.
[23] Zheng, Y. K.; Wang, X. M.; Jiang, H. Label-free detection of *Acinetobacter baumannii* through the induced fluorescence quenching of thiolated AuAg nanoclusters. *Sens. Actuators B: Chem.* **2018**, *277*, 388–393.
[24] Ahmed, H. B. Recruitment of various biological macromolecules in fabrication of gold nanoparticles: Overview for preparation and applications. *Int. J. Biol. Macromol.* **2019**, *140*, 265–277.
[25] Erythropel, H. C.; Zimmerman, J. B.; de Winter, T. M.; Petitjean, L.; Melnikov, F.; Lam, C. H.; Lounsbury, A. W.; Mellor, K. E.; Janković, N. Z.; Tu, Q. S. et al. The Green ChemisTREE: 20 years after taking root with the 12 principles. *Green Chem.* **2018**, *20*, 1929–1961.
[26] Basu, T.; Rana, K.; Das, N.; Pal, B. Selective detection of Mg^{2+} ions via enhanced fluorescence emission using Au-DNA nanocomposites. *Beilstein J. Nanotechnol.* **2017**, *8*, 762–771.
[27] Li, X. M.; Fu, P. Y.; Liu, J. M.; Zhang, S. S. Biosensor for multiplex detection of two DNA target sequences using enzyme-functionalized Au nanoparticles as signal amplification. *Anal. Chim. Acta* **2010**, *673*, 133–138.
[28] Xiu, W. J.; Gan, S. Y.; Wen, Q. R.; Qiu, Q.; Dai, S. L.; Dong, H.; Li, Q.; Yuwen, L. H.; Weng, L. X.; Teng, Z. G. et al. Biofilm microenvironment-responsive nanotheranostics for dual-mode imaging and hypoxia-relief-enhanced photodynamic therapy of bacterial infections. *Research* **2020**, *2020*, 9426453.
[29] Xu, S. Y.; Yin, W.; Zhang, Y. L.; Lv, Q. M.; Yang, Y. J.; He, J. Foes or friends? Bacteria enriched in the tumor microenvironment of colorectal cancer. *Cancers* **2020**, *12*, 372.
[30] Nothling, M. D.; Cao, H. W.; McKenzie, T. G.; Hocking, D. M.; Strugnell, R. A.; Qiao G. G. Bacterial redox potential powers controlled radical polymerization. *J. Am. Chem. Soc.* **2021**, *143*, 286–293.
[31] Jena, S.; Das, B.; Bosu, R.; Suar, M.; Mandal, D. Bacteria generated antibacterial gold nanoparticles and potential mechanistic insight. *J. Cluster Sci.* **2015**, *26*, 1707–1721.
[32] Song, C. X.; Xu, J. Y.; Chen, Y.; Zhang, L. L.; Lu, Y.; Qing, Z. H. DNA-templated fluorescent nanoclusters for metal ions detection. *Molecules* **2019**, *24*, 4189.
[33] Zhao, C. Q.; Du, T. Y.; ur Rehman, F.; Lai, L. M.; Liu, X. L.; Jiang, X. R.; Li, X. Q.; Chen, Y.; Zhang, H.; Sun, Y. et al. Biosynthesized gold nanoclusters and iron complexes as scaffolds for multimodal cancer bioimaging. *Small* **2016**, *12*, 6255–6265.
[34] Schwartz-Duval, A. S.; Konopka, C. J.; Moitra, P.; Daza, E. A.; Srivastava, I.; Johnson, E. V.; Kampert, T. L.; Fayn, S.; Haran, A.; Dobrucki, L. W. et al. Intratumoral generation of photothermal gold nanoparticles through a vectorized biomineralization of ionic gold. *Nat. Commun.* **2020**, *11*, 4530.
[35] Wang, M. N.; Chen, Y.; Cai, W. J.; Feng, H.; Du, T. Y.; Liu, W. W.; Jiang, H.; Pasquarelli, A.; Weizmann, Y.; Wang, X. M. *In situ* self-assembling Au-DNA complexes for targeted cancer bioimaging and inhibition. *Proc. Natl. Acad. Sci. USA* **2020**, *117*, 308–316.
[36] Liu, J. W. DNA-stabilized, fluorescent, metal nanoclusters for biosensor development. *TrAC Trends Anal. Chem.* **2014**, *58*, 99–111.
[37] Zhao, W. H.; Xiong, M.; Liu, M. B.; Wang, S. Q.; Xian, X.; Lin, B. P.; Li, H. B. Evaluation of the effect of Tb(IV)-NR complex on herring sperm DNA genetic information by mean of spectroscopic. *Nucleosides Nucleotides Nucleic Acids* **2020**, *39*, 964–978.
[38] Szymborska-Małek, K.; Komorowska, M.; Gąsior-Głogowska, M. Effects of near infrared radiation on DNA. DLS and ATR-FTIR study. *Spectrochim. Acta A:Mol. Biomol. Spectrosc.* **2018**, *188*, 258–267.
[39] Kallistova, A. Y.; Nikolaev, Y. A.; Mardanov, A. V.; Berestovskaya, Y. Y.; Grachev, V. A.; Kostrikina, N. A.; Pelevina, A. V.; Ravin, N. V.; Pimenov, N. V. Investigation of formation and development of anammox biofilms by light, epifluorescence, and electron microscopy. *Microbiology* **2020**, *89*, 708–719.
[40] Zheng, Y. K.; Liu, W. W.; Chen, Y.; Li, C. M.; Jiang, H.; Wang, X. M. Conjugating gold nanoclusters and antimicrobial peptides: From aggregation-induced emission to antibacterial synergy. *J. Colloid Interface Sci.* **2019**, *546*, 1–10.
[41] Zheng, K. Y.; Setyawati, M. I.; Leong, D. T.; Xie, J. P. Overcoming bacterial physical defenses with molecule-like ultrasmall antimicrobial gold nanoclusters. *Bioact. Mater.* **2021**, *6*, 941–950.
[42] Zheng, Y. K.; Liu, W. W.; Qin, Z. J.; Chen, Y.; Jiang, H.; Wang, X. M. Mercaptopyrimidine-conjugated gold nanoclusters as nanoantibiotics for combating multidrug-resistant superbugs. *Bioconjugate Chem.* **2018**, *29*, 3094–3103.
[43] Chevallier, E.; Jolibois, R. D.; Meunier, N.; Carlier, P.; Monod, A. "Fenton-like" reactions of methylhydroperoxide and ethylhydroperoxide with Fe^{2+} in liquid aerosols under tropospheric conditions. *Atmos. Environ.* **2004**, *38*, 921–933.
[44] Zayats, M.; Baron, R.; Popov, I.; Willner, I. Biocatalytic growth of Au nanoparticles: From mechanistic aspects to biosensors design. *Nano Lett.* **2005**, *5*, 21–25.
[45] Iakimov, N. P.; Abdullina, V. R.; Sharanov, P. A.; Alov, N. V.;

Orlov, V. N.; Grozdova, I. D.; Melik-Nubarov, N. S. Interaction of glutathione-stabilized gold nanoclusters with doxorubicin and polycation. *Russ. J. Gen. Chem.* **2019**, *89*, 2097–2102.

[46] Gang, G. T.; Kim, Y. H.; Noh, J. R.; Kim, K. S.; Jung, J. Y.; Shong, M.; Hwang, J. H.; Lee, C. H. Protective role of NAD(P)H: Quinone oxidoreductase 1 (NQO1) in cisplatin-induced nephrotoxicity. *Toxicol. Lett.* **2013**, *221*, 165–175.

[47] Hoshino, Y.; Mizuno, S.; Kato, K.; Mizuno-Iijima, S.; Tanimoto, Y.; Ishida, M.; Kajiwara, N.; Sakasai, T.; Miwa, Y.; Takahashi, S. et al. Simple generation of hairless mice for *in vivo* imaging. *Exp. Anim.* **2017**, *66*, 437–445.

[48] Tran, M. T. N.; Tanaka, J.; Hamada, M.; Sugiyama, Y.; Sakaguchi, S.; Nakamura, M.; Takahashi, S.; Miwa, Y. *In vivo* image analysis using iRFP transgenic mice. *Exp. Anim.* **2014**, *63*, 311–319.